Optical Implications of Crystallite Symmetry and Structure in Potassium Niobate Tellurite Glass Ceramics

Robert T. Hart, Jr., Matthew A. Anspach, Brian J. Kraft, Jeffrey M. Zaleski, and Josef W. Zwanziger*

Department of Chemistry, Indiana University, Bloomington, Indiana 47405

Peter J. DeSanto

W. M. Keck Electron Microscopy Facility, Spencer Laboratory, University of Delaware, Wilmington, Delaware 19716

Barry Stein

Indiana Molecular Biology Institute, Indiana University, Bloomington, Indiana 47405

Jaby Jacob and P. Thiyagarajan

Intense Pulsed Neutron Source, Argonne National Laboratory, Argonne, Illinois 60439

Received June 5, 2002. Revised Manuscript Received August 20, 2002

We present combined results of optical, scattering, and spectroscopic studies of $(K_2O)_{15}(Nb_2O_5)_{15}(TeO_2)_{70}$ glass and glass ceramic and comment on possible mechanisms of the optical behavior in terms of existing theory. The glass ceramic is confirmed to generate second-harmonic light. Combined neutron and X-ray diffraction data have been indexed to an orthorhombic unit cell ($a = 3.39$ Å, $b = 4.78$ Å, $c = 6.38$ Å). Additionally, we show that the previously proposed fluorite-based model is insufficient for the crystal phase using real-space analysis. The orthorhombic unit cell allows the possibility of a conventional explanation for the second-harmonic generation (SHG). Peak broadening and scattering length difference analyses are combined to formulate a model of anion disorder in the crystal phase. TEM and SAXS reveal domains of ≈15 nm in both the glass and glass ceramic. The role of liquid−liquid phase separation in the crystallization behavior of this material is discussed. Solid-state ^{93}Nb MAS NMR and Raman spectroscopy offer insight into Te valence and polyhedral distribution as well as Nb site symmetry and chemical connectivity. The effects of these geometries and anion disorder on optical response are discussed.

1. Introduction

Glasses and glass ceramics with nonlinear optical (NLO) properties possess many attractive features compared to those of crystalline materials used in the same application. Optical devices often have to perform under environmentally harsh conditions and must be fabricated to exacting shapes. Oxide glasses are chemically durable and can be drawn or molded into almost any shape. However, because of inherent inversion symmetry, a homogeneous glass cannot exhibit any characteristics of even terms of nonlinear optical response, including second-harmonic generation (SHG) and sum frequency generation (SFG).[1] Glass ceramics break this symmetry restriction when the ceramic phase does not have a center of inversion.

The applications for moldable transparent nanostructured SHG materials are under investigation. The minute size of the crystallites may offer novel advantages in material applications. For example, short laser pulses have considerable dispersion in their frequency. When passed through doubling crystals, shape and frequency components of the doubled pulse are altered because of different phase velocities of the waveform. The current strategy is to use a very thin section of potassium titanyl phosphate (KTP) or lithium niobate to approach the sin $\theta = \theta$ regime for all colors.[2] However, with nanostructured materials, this condition is met for each crystallite and we propose that only a small dispersion will accumulate. Additionally, if the crystallite orientation can be influenced with an external field during growth, the possibility of phase matching exists. Low-cost waveguides and doubling "crystals" could be manufactured from these materials.

* To whom correspondence should be addressed. Tel.: (812) 855-3994. Fax: (812) 855-8300. E-mail: jzwanzig@indiana.edu.

(1) *Principles and Applications of Nonlinear Optical Materials*, 1st ed.; Munn, R. W., Ironside, C. N., Eds.; Blackie Academic and Professional: Boca Raton, FL, 1993; p 257.

(2) Dantus, M. *Annu. Rev. Phys. Chem.* **2001**, *52*, 639.

10.1021/cm020615q CCC: $22.00
Published on Web 10/01/2002

Some reports of this type of glass ceramic have appeared recently.[3−5] However, the report of a tellurite glass ceramic has generated considerable interest in the field since it was also reported to generate strong SHG, similar to quartz.[6−9] Tellurites are desirable for applications due to their exceptional chemical durability. The reported tellurite glass ceramic is particularly intriguing, however, because it was reported to have a fluorite crystalline phase.[7] A fluorite-type phase cannot produce SHG since it is has a center of inversion (space group $Fd\bar{3}m$). The observations reported for this material were therefore puzzling and suggested the possibility of various exotic mechanisms of nonlinear optical response. The current report contains the results of optical measurements confirming that this material is in fact SHG-active and crystallographic results that reject the fluorite model and support a more conventional mechanism.

The atomistic mechanism responsible for the NLO is, we believe, the presence of distorted metal oxide polyhedra and the existence of anion disorder in the crystal structure. We show evidence for both types of structures using the diffraction profiles and NMR and Raman spectroscopies. This atomistic mechanism of SHG is consistent with the model of NLO behavior in d-metal oxides advanced by Lines.[10−12]

The formation of crystallites from a glass is a kinetically complex process driven initially by phase separation. We show by SAXS and TEM that binodal phase separation has already occurred in the glass. This leads to the rapid formation of crystallites in the droplet phase at the heat treatment temperature. This microstructure affects the crystallites in that the size of the droplet domain determines the final size of the crystallite.

2. Experimental Methods

Sample Preparation. Glass samples were synthesized by the melt quench method described by Shioya et al. from reagent-grade K_2CO_3, Nb_2O_5, and TeO_2 from either Alfa Æsar (Ward Hill, MA) or Aldrich (Milwaukee, WI).[6] Glass ceramics were prepared by treating glasses at 425 °C for times up to 168 h (specified in text where appropriate).

SHG Verification. Optical measurements were made of the frequency, time, and power response of a sample heat-treated for 168 h. The sample was irradiated with the fundamental of a Nd^{3+}/YAG laser Q-switched at 10 Hz with an average pulse width of 11 ns. The sample surface was oriented reproducibly with an $xyz\theta$ stage 45° to the incident beam. The signal was collected orthogonally to the source with condensing optics and submitted to three short pass filters at 700, 650, and 600 nm to remove scattered fundamental (Figure 1). The doubled frequency at 532 nm was selected with a Spex 340S 20-cm monochromator (1200 grooves/mm, 500-nm blaze)

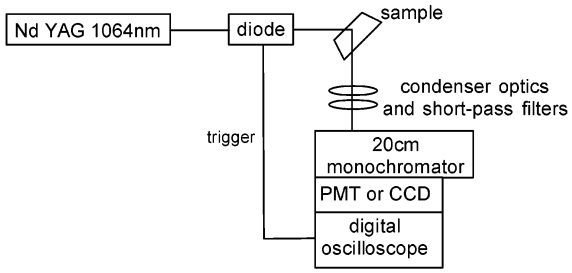

Figure 1. Experimental setup for measuring the temporal, frequency, and power dependence of SHG from glass ceramic samples.

and quantified with a Hamatsu R928 PMT. To measure the frequency response, the monochromator output was dispersed across a Roper Scientific CCD.

Wide-Angle Scattering and Unit Cell Analysis. Powder X-ray diffraction data were collected at the BM-1 station of SRI-CAT at the Advanced Photon Source of Argonne National Laboratory using 18.83 kV of radiation in $\theta-2\theta$ geometry or with a Bruker AXS SMART 6000 system with a Mo Kα source in transmission geometry. The latter X-ray data were transformed to real space with the RAD program.[13] Powder neutron diffraction data were collected on the GPPD[14] and GLAD[15] instruments at the Intense Pulsed Neutron Source at Argonne National Laboratory. The GLAD data were reduced and analyzed following the procedure using the software package developed at the laboratory. The combined peak list from powder X-ray and GPPD study is used in the program Crysfire[16] to search for candidate unit cells. Due to the small number of reflections, only the programs Taup,[17] Treor,[18] and Dicvol[19] could be used. Peak-broadening analysis was done by subtracting a linear background from the region of the peak and then fitting the shape with a five-parameter pseudo-Voigt function using the nonlinear least-squares fitting module of Origin 6.0.[20] The peak regions were defined as widely as possible to avoid apodization effects, and overlapping peaks were fit simultaneously.

Texture Analysis: TEM and SAXS. TEM images were obtained on a JEOL 1010 at 60 kV or a JEOL 2010 F with a field emission source at 200 kV by either suspending powders of the samples in Spi-Pon resin on copper grids or by dropping a suspension of the sample powder in acetone onto a lacey-carbon film coated copper sample grid and allowing the suspendant to evaporate. X-ray microanalysis was done using an EDAX Phoenix energy-dispersive X-ray spectrometer. The Scion Image software was used to enhance contrast and analyze particle sizes. The small-angle X-ray scattering instrument has a rotating anode source, which emits copper K_α radiation at a wavelength of 1.54 Å. The beam size at the sample position was reduced to approximately 1 × 1 mm by a set of focusing slits. The samples in powdered form were sandwiched between two Kapton films and mounted on an aluminum sample holder. The thickness of each sample was <0.1 mm. The detector was mounted ≈2.5 m from the sample position and allowed intensity measurements over the range $0.01 \le q \le 0.25$ Å^{-1}. The scattered intensity was measured by a multiwire gas detector (18 × 18 cm). The intensity of the transmitted beam was measured simultaneously using a

(3) Pernice, P.; Aronne, A.; Sigaev, V.; Kupriyanova, M. *J. Non-Cryst. Solids* **2000**, *275*, 216.
(4) Murugan, G. S.; Varma, K. B. R. *J. Non-Cryst. Solids* **2001**, *279*, 1.
(5) Yamamoto, Y.; Nasu, H.; Hashimoto, T.; Kamiya, K. *J. Non-Cryst. Solids* **2001**, *281*, 198.
(6) Shioya, K.; Komatsu, T.; Kim, H. G.; Sato, R.; Matusita, K. *J. Non-Cryst. Solids* **1995**, *189*, 16.
(7) Kim, H. G.; Komatsu, T.; Shioya, K.; Matusita, K.; Tanaka, K.; Hirao, K. *J. Non-Cryst. Solids* **1996**, *208*, 303.
(8) Komatsu, T.; Shioya, K. *J. Non-Cryst. Solids* **1997**, *209*, 305.
(9) Sakai, R.; Benino, Y.; Komatsu, T. *Appl. Phys. Lett.* **2000**, *77*, 2118.
(10) Lines, M. E. *Phys. Rev. B* **1991**, *43*, 11978.
(11) Lines, M. E. *Phys. Rev. B* **1990**, *41*, 3372.
(12) Lines, M. E. *Phys. Rev. B* **1990**, *41*, 3383.
(13) Petkov, V. *J. Appl. Crystallogr.* **1989**, *22*, 387.
(14) Jorgensen, J. D.; Faber, J.; Carpenter, J. M.; Crawford, R. K.; Haumann, J. R.; Hitterman, R. L.; Kleb, R.; Ostrowski, G. E.; Rotella, F. J.; Worlton, T. G. *J. Appl. Crystallogr.* **1989**, *22*, 321.
(15) Ellison, A. J. G.; Crawford, R. K.; Montague, D. G.; Volin, K. J.; Price, D. L. *J. Neutron Res.* **1993**, *1*, 61.
(16) Shirley, R. *The CRYSFIRE System for Automatic Powder Indexing: User's Manual*; The Lattice Press: Surrey, 2000.
(17) Taupin, D. *J. Appl. Crystallogr.* **1973**, *6*, 380.
(18) Werner, P.-E.; Eriksson, L.; Westdahl, M. *J. Appl. Crystallogr.* **1985**, *18*, 367.
(19) Boultif, A.; Louer, D. *J. Appl. Crystallogr.* **1991**, *24*, 987.
(20) Wertheim, G. K.; Butler, M. A.; West, K. W.; Buchanan, D. N. E. *Rev. Sci. Instrum.* **1974**, *45*, 1369.

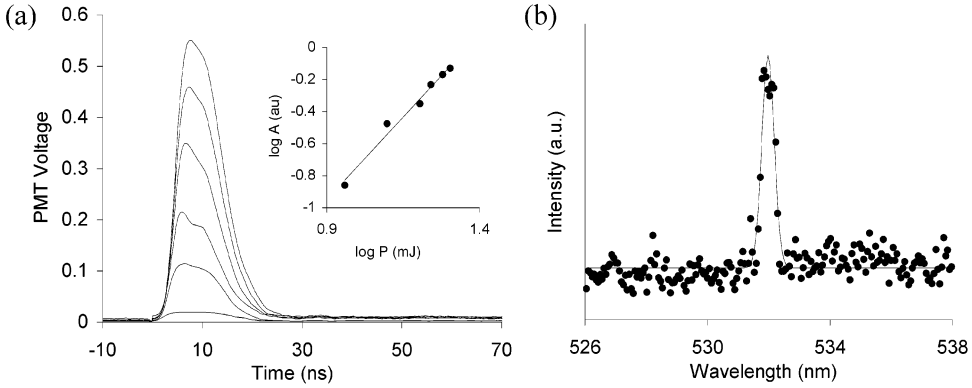

Figure 2. (a) Temporal and power dependence of 532-nm light from the glass ceramic with 1064-nm incident laser pulse at $t = 0$. The laser power is varied from experiment to experiment. In order of increasing peak 532-nm intensity, the powers are 9.1, 12.5, 16.0, 17.4, 19.0, and 20.1 mJ/pulse. Inset: log−log plot of peak amplitude vs pulse power. The best-fit slope is 2.06. (b) Intensity of generated light as a function of wavelength (points) with Gaussian fit (line) of fwhm = 0.8 nm.

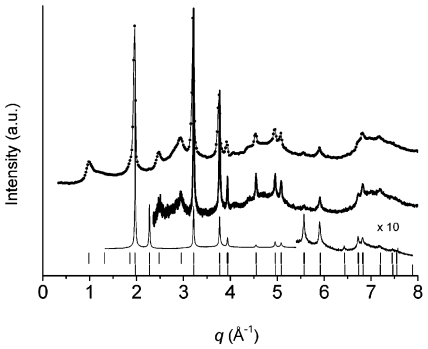

Figure 3. Three scattering data sets used in the indexing of the crystalline phase of the glass ceramic. Lower tics, cubic cell predicted reflections; upper tics, orthorhombic cell predicted reflections; solid line, X-ray; bold line, GPPD; dotted line, GLAD.

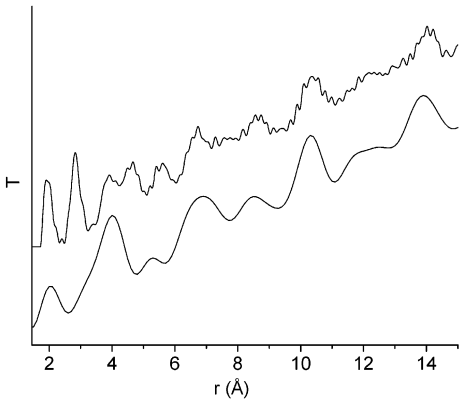

Figure 4. Dimensionless total correlation function, $T(r)$, for neutron diffraction data (upper) and X-ray diffraction data (lower).

photodiode to account for the fluctuations in the incident beam intensity and the absorption of X-rays by the sample. The two-dimensional intensity pattern was azimuthally averaged to produce the $I(q)$ vs q plots. The scattering from the tapes was subtracted from the total intensity to obtain the pattern of the sample independently.

Polyhedral Structure: NMR and Raman Spectroscopies. Solid State ^{93}Nb NMR was taken at 98.6 MHz under an applied field of 9.4 T on a Bruker Avance spectrometer. A 2.5-mm HPMB MAS probe was used with RF field strength of 25 kHz. Spectra were collected with a rotor synchronized Hahn echo pulse sequence. Spectra were referenced externally to the sharp resonance of $NbCl_5$ in MeCN (0 ppm). The typical delay between pulses was $4\tau_r$, where τ_r is the rotor period of 33 μs. Time signals were multiplied by a Gaussian of width 1000 Hz centered on the echo. The recycle delay was at least $5T_1$, typically 1 s. Spectra were accumulated to roughly equivalent S/N ratios, requiring ≈2000 scans for the crystalline materials and ≈12 000 scans for the glass and glass ceramic. Raman spectra were acquired with a Renishaw RM2000 Raman microscope with a 785-nm diode laser as the excitation source. Samples were heated with a Linkam FTIR 600 variable temperature microscope stage.

3. Results

Figure 2 shows the results of the optical measurements of the light emanating from the glass ceramic while under irradiation by a 1064-nm laser source. Figure 3 contains scattering data normalized to the highest intensity feature in each pattern. The list of peak positions (Table 1) is determined by fitting the peaks with the pseudo-Voigt function (see below) and using the least-squares refined value for peak center. The unit cell indexing programs Treor, Dicvol, and Taup find an orthorhombic cell of $a = 3.39$ Å, $b = 4.78$ Å, and $c = 6.38$ Å. This is the only cell that all three programs find, and it has the highest figure of merit of any candidate cell proposed by any of the programs.

Table 1. Observed and Predicted Peak Positions

d_{obs} (Å)	d_{pred} (Å)	d_{obs} (Å)	d_{pred} (Å)	d_{obs} (Å)	d_{pred} (Å)
6.411	6.388	1.594	1.595	0.977	0.976
3.186	3.194	1.380	1.381	0.934	0.933
2.761	2.762	1.267	1.267	0.921	0.921
2.530	2.535	1.235	1.236	0.873	0.872
2.138	2.129	1.127	1.128	0.842	0.843
1.952	1.951	1.061	1.062	0.832	0.832
1.665	1.665				

The relationship between the observed corrected structure factor ($S(Q)$) and the total correlation function ($T(r)$) is[21]

$$T(r) = 4\pi r\rho_0 + \frac{2}{\pi}\int_0^\infty Q(S(Q) - 1)\sin Qr \, dQ$$

The differences between the neutron and X-ray functions arise from the different scattering lengths for the two experiments. Results are shown in Figure 4.

The SAXS result from the glass as quenched is shown in Figure 5. The results from the other samples are

(21) Elliott, S. R. *Physics of Amorphous Materials*, 2nd ed.; Oxford University Press: Oxford, 1990.

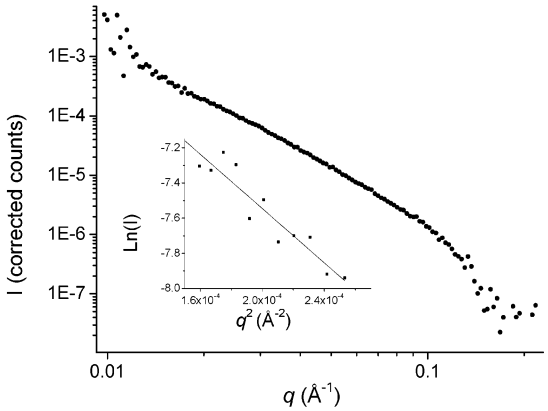

Figure 5. SAXS data for as-quenched glass. Inset: Guinier fit of low q data with $r = 19.6 \pm 1.2$ nm.

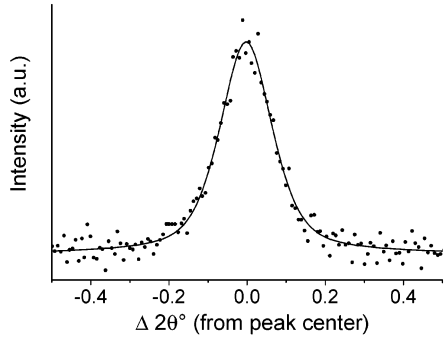

Figure 6. Pseudo-Voigt function fit of the peak appearing at 3.94 $Å^{-1}$ in the 144° bank of GPPD. From this figure it is clear that fitting was needed to accurately determine the peak center positions (see text).

Table 2. Results of Guinier Analysis of SAXS Data (Error Refers to the Fit, Not to the Particle Size Distribution)

sample	r (nm)	sample	r (nm)
glass	19.6 ± 1.2	70 h	19.0 ± 1.0
4 h	20.5 ± 1.3	168 h	18.0 ± 1.2
14 h	18.6 ± 0.9		

Table 3. Gaussian and Lorentzian Components of the Peak Broadening

peak position (d spacing)	Gaussian width	Lorentzian width
3.188	0.116	0.080
2.860	0.100	0.112
2.523	0.503	0.092
2.131	0.543	0.079
1.953	0.097	0.137
1.665	0.191	0.173
1.595	0.101	0.091
1.380	0.143	0.123
1.063	0.078	0.512

similar, and the results of Guinier analyses are collected in Table 2. An example of the peak broadening analysis is shown in Figure 6. The important results for this work are the Γ_G and Γ_L, the Gaussian and Lorentzian components of the line broadening, respectively. These values are collected in Table 3. A graph of the two breadths as a function of d spacing is shown in Figure 7 as well as the predicted Lorentzian broadening according to the Von Laue formula for dilute monodisperse spherical particles of 14.4-nm diameter. This is the diameter of the particles in the glass ceramic found by measuring their sizes in the TEM images.

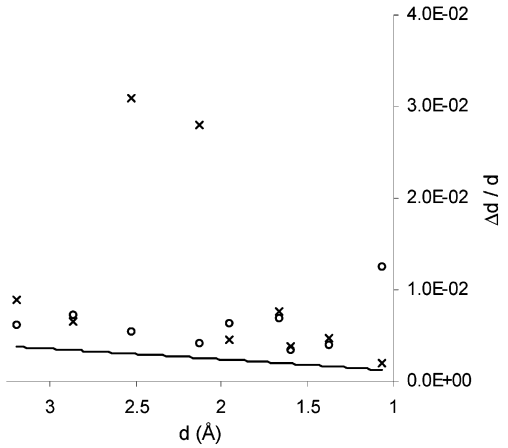

Figure 7. Results of pseudo-Voigt fits showing Gaussian (× symbols) and Lorentzian components (circles) for the glass ceramic. The line shows the expected Lorentzian broadening for spherical crystallites of 14.4-nm diameter.

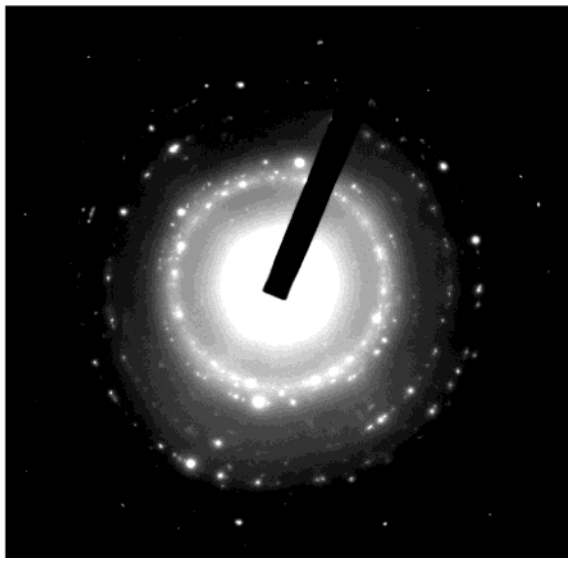

Figure 8. Electron diffraction pattern of the glass ceramic.

The area electron diffraction pattern (SAED) shown in Figure 8 was taken at a camera length of 80 cm from several thin particles. The first five intense diffraction rings yield d-spacings of 3.19, 2.79, 1.98, 1.70, and 1.63 Å. Weaker diffraction rings were also observed at 6.04, 4.44, 3.08, 2.23, 1.82, 1.34, 1.29, and 1.25 Å. A bright field image and a dark field image obtained from the 3.19-Å diffraction ring are shown in Figure 9. X-ray microanlaysis indicates that the crystalline regions have higher amounts of K and Nb than the surrounding amorphous region. However, the chemical composition of the crystallites could not be absolutely determined because of their small size. Figure 10 is a TEM image of the glass as quenched.

NMR results are shown in Figure 11. Raman spectra are collected in Figure 12.

4. Discussion

Formation of the Glass Ceramic. The bulk glass formed by quenching the melt shows no X-ray scattering indicative of crystalline order and shows one glass transition event in differential scanning calorimetry at 395 °C. Heat treatment at 425 °C induces growth of

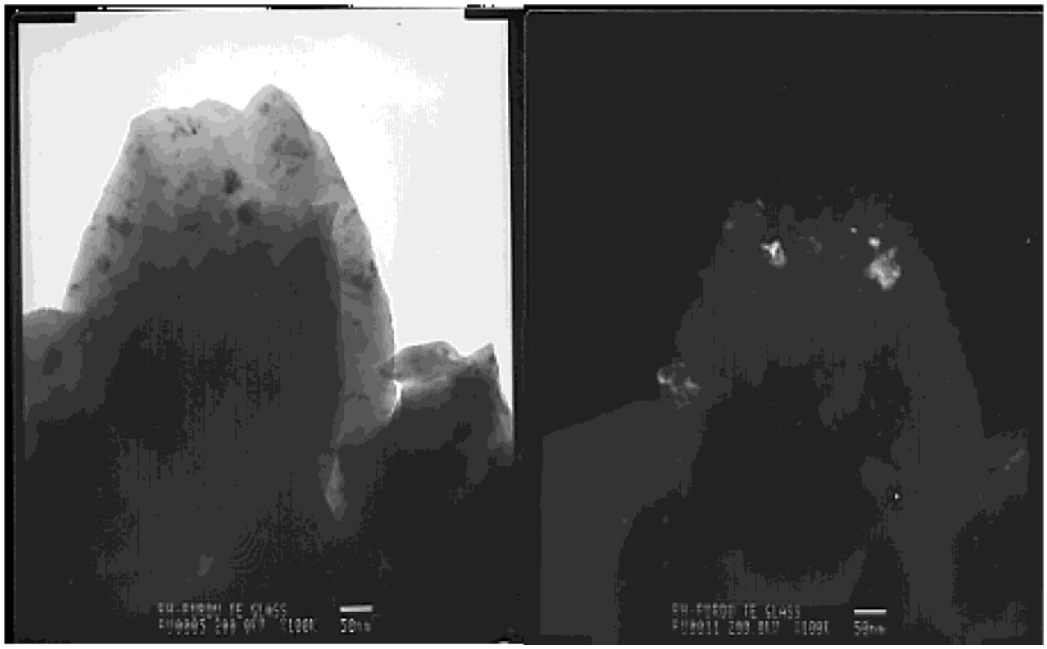

Figure 9. Left: bright field TEM image of the glass ceramic. Right: dark field image.

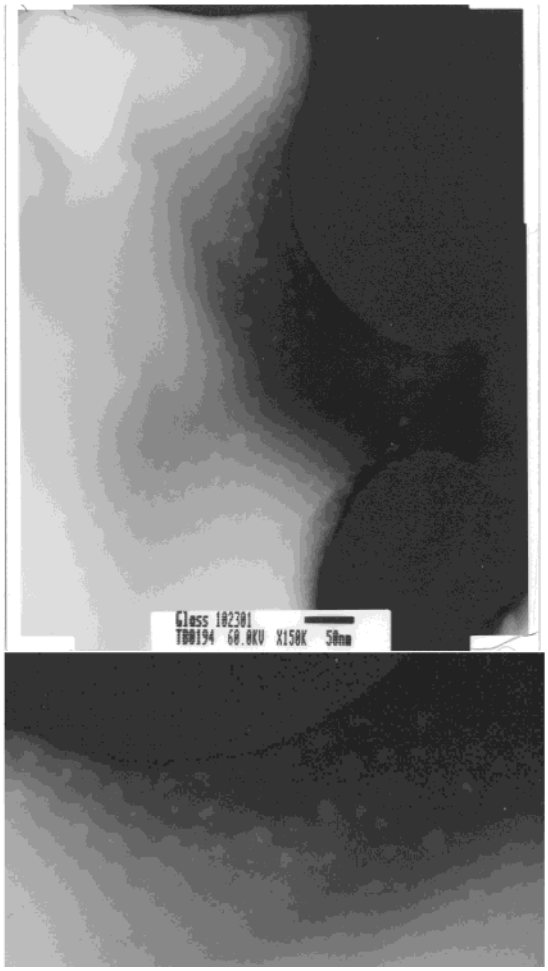

Figure 10. Above: TEM of as-quenched glass. Below: Close-up of powder grain edge.

crystalline particles in the glass, which show Bragg peaks in diffraction. The color of the sample changes from pale yellow to orange-yellow upon heat treatment, consistent with the previously published optical absorption measurements.[7]

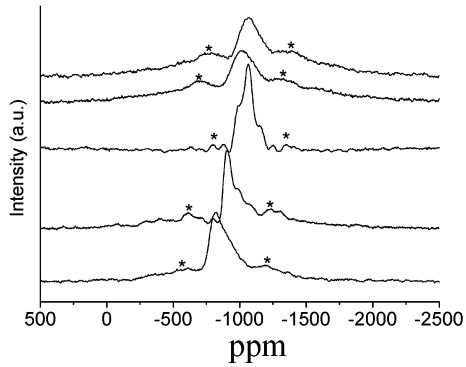

Figure 11. Solid state ^{93}Nb MAS NMR of niobates. From top to bottom: glass ceramic, glass, Nb_2O_5, $KNbO_3$, and $KTeNbO_6$. Spectra are collected at 30 kHz; asterisks indicate spinning side bands.

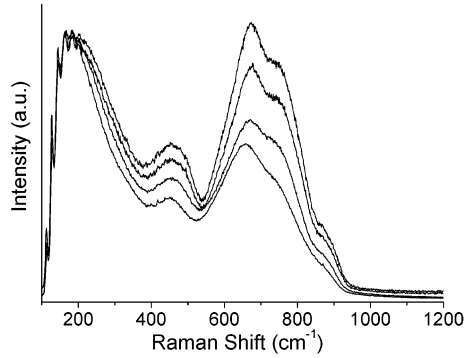

Figure 12. Raman spectra of glass during heat treatment. From top to bottom: as-quenched, 100 °C, 2 h @ 425 °C, and 3 h @ 425 °C.

Optical Response. The optical response (Figure 2) shows that the green light emanating from the sample is SHG. The signal has similar width in time to the incident laser (11-ns laser pulse) and the signal amplitude scales with the incident laser power squared within the scatter of the data. This is a consequence of the $\chi^{(2)} \cdot E^2$ term in the nonlinear polarization equation. The

structures that could give rise to this term and evidence for their presence will be examined below.

Bragg Peaks and Unit Cell. Previous work on this material using a laboratory-based wide-angle X-ray diffraction instrument revealed only five Bragg peaks from the glass ceramic.[6] The observed pattern was fit to an FCC cell with $a = 5.54$ Å. However, because the scattering cross section of X-rays from oxygen is small relative to that from niobium and tellurium, X-ray diffraction alone is often insufficient to characterize the structure of metal oxide materials. On the other hand, neutrons scatter from oxygen rather strongly, with a cross section similar to that of tellurium (5.803 barns vs 5.80 barns). From the neutron diffraction data we observed the presence of three additional broad, low-angle Bragg reflections. These peaks do not fit the previously assigned FCC cell. The $\sin^2\theta$ of the first peak ($q = 0.98$ Å^{-1}) is one-quarter the $\sin^2\theta$ of the second peak, suggesting a cubic superlattice of $a = 11.08$ Å, but the peaks at $q = 2.48$ and 2.95 Å^{-1} do not fit a cubic pattern. By fitting all the Bragg peaks found in X-ray diffraction and neutron diffraction (19 total) using the programs Treor, Dicvol, and Taup, a primitive orthorhombic unit cell with parameters $a = 3.39$ Å, $b = 4.78$ Å, and $c = 6.38$ Å was found. The DeWolff criterion for this cell was 10.0, as compared to a value of 5.4 for the FCC cell.[22] However, when considering these two figures, one should bear in mind that the cubic system leaves three of the low-angle peaks unindexed. If the crystal structure can be determined and refined, it will be possible to know the exact crystal system parameters (and in addition the Bragg peak intensities, which cannot be calculated from only the unit cell parameters). Given the small size of the crystallites and the strong diffuse background of the glass matrix, the standard index-assignment-completion-refinement algorithm for powder samples cannot be applied.[23] Therefore, the unit cell assignment will remain ambiguous.

When Figure 3 is examined, some comments can be made about the observed and predicted reflections. The cubic cell predicts all the peaks in the X-ray diffraction data, but the second predicted reflection has almost no intensity in the neutron diffraction patterns. Additionally, the X-ray patterns do not show the first, second, third, sixth, or seventh predicted reflection for the orthorhombic cell. The second and third peaks are not resolved in the GLAD data, but the intensity of the first peak trails off toward the second predicted reflection, and the second peak has a shoulder toward the third predicted reflection. This is also approximately where a weak ring appears in the SAED pattern (4.44 Å).[24] The base reflections are the first, fourth, fifth, sixth, seventh, and eighth reflections, suggesting that peaks from both the metal framework and the oxide structure within the crystallites are important in describing the unit cell. It should be noted that the DeWolff figure of merit contains a factor of n_o/n_p, where n_o is the number of observed peaks and n_p is the number of "possible" peaks for the predicted cell. Since the indexing programs simply cut out at an arbitrary, used defined delta from the peak center, it is implicitly assumed that all other regions of the pattern are zero and that all peaks are resolvable. There are many predicted reflections with nonzero intensity (i.e., they are predicted to be beneath the peak tails); however, the DeWolff figure does not provide any means to account for this. Nevertheless, the DeWolff figure provides useful relative guides to candidate indexings of a powder pattern.

Unfortunately, determination of the lattice parameters does not answer the question of whether the structure possesses inversion symmetry and is thus forbidden by this symmetry from exhibiting SHG. For instance, the face-centered cubic cell assigned in earlier work admits multiple possibilities for the space group, some of which do not include inversion symmetry; likewise, the orthorhombic cell determined here from a much more complete data set admits space groups with inversion symmetry. On the other hand, the fluorite model proposed previously does have inversion symmetry and thus requires an exotic mechanism to show SHG; it cannot be rejected solely on this account, however. In the following we will discuss the inconsistency of the fluorite model with our data and then go on to illustrate elements of the structure that can in fact account for the optical response of the material in a simple way.

In the fluorite structure with $a = 5.54$ Å, the first M−O distance is 2.4 Å, but typical M−O bond lengths in niobates and tellurites are ≤2.2 Å. Further, there is a *minimum* in the experimental total correlation function at 2.4 Å and a maximum at 2.0 Å, indicating that the true crystal structure has typical bond lengths, not the 2.4 Å as required by the fluorite model (Figure 4). Furthermore, in a fluorite cell, each cation is coordinated by eight anions, while in all known niobates, Nb^{5+} is coordinated by six oxides. Likewise, in the IV state, Te commonly includes three or four oxide ions in its first valence. To our knowledge, there is no precedent of cubic coordination for either of these ions. Additionally, the stoichiometry determined by EDX in the previous work suggests an oxygen deficiency of about 1.6 atoms per unit cell for the fluorite structure, which seems rather high. The distortions necessary to accommodate these issues would be large enough to break some of the symmetries and be observed in the X-ray diffraction pattern.

We cannot propose a crystal structure for the ceramic phase in this work using the data acquired so far. However, the X-ray diffraction pattern is consistent with a cubic closest packed arrangement of metal ions. So while the metal ions may be arranged in a way that has inversion symmetry (assuming that they are regularly arranged), the anions need not be. In fact, considering the usual geometries of tellurites and niobates, it is difficult to imagine a cubic unit cell that would accommodate this material's stoichiometry. And indeed, the orthorhombic cell is a much better fit for all the observed peaks. The point to be made is that polarizability and hyperpolarizabilities do not depend on the core electrons of the metals that cause the X-ray diffraction pattern. The optical properties depend on the valence electrons and the arrangements of the bonds, in other words, the oxide positions in the repeating structure.

(22) DeWolff, P. M. *J. Appl. Crystallogr.* **1968**, *1*, 108.
(23) McCusker, L. B.; Von Dreele, R. B.; Cox, D. E.; Louer, D.; Scardi, P. *J. Appl. Crystallogr.* **1999**, *32*, 36.
(24) This can also be assigned to a superstructure.

Anion Disorder Model. We have used a pseudo-Voigt function to fit the peak profiles and interpreted the Lorentzian broadening as due to small particle size and the Gaussian broadening as evidence of microstrain.[25] We understand that this method cannot be used a priori to determine crystallite features, but it can be used to first order in the presence of other confirming information about the sample microstructure and instrumental broadening function. For the APS and GPPD instruments, the instrumental broadening is at least an order of magnitude smaller than the small-particle size broadening. The reasonably good fit of the Lorentzian (Figure 5) broadening to the predicted curve is interpreted as support for this treatment. From the fits, it is seen that the two peaks that do not appear in the X-ray diffraction patterns contain a much larger Gaussian component to their shapes than the others. As an aside, Figure 6 demonstrates the usefulness of this technique for determining the peak centers. Considering that the scattering lengths scale the partial structure factors, we can conclude that these reflections occur from planes containing predominantly oxide anions. We interpret this broadening as evidence of randomness in anion position. Distortion from equilibrium bond length leads to anomalous polarization and hyperpolarizability. Thus, this anion disorder model helps to explain the generation of SHG in the glass ceramic as well.

Microstructure and Material Evolution. Guinier analysis of the SAXS data of the glass reveals electron density fluctuations on the scale of 19 nm (Figure 5, Table 2). The direct observation of this structure by TEM points to liquid−liquid phase separation in the melt. The circular shape of the particles in the micrograph of the glass (Figure 10) is typical of binodal phase separation. This is a common phenomenon among glasses that form glass ceramics.[26] We postulate that the crystalline phase precipitates from the droplet phase in the glass. This explains the small size of the particles and the large amount of microstrain in them. When the droplets crystallize, they cannot grow larger, regardless of heat treatment time, because the composition of the matrix glass is too far from the crystals', and they are strained because they must be continuous with the glass. The evidence for this is in Table 2, showing that the particle radius does not change appreciably with heat treatment time.

The bright field and dark field TEM images (Figure 9) offer some interesting insights into the nature of the crystallites. In the bright field image, all the crystallites show up as dark areas. In the dark field images, only those crystallites with a particular orientation show up as bright areas. It can be seen that several of the crystallites have this orientation, but several areas that are clearly crystallites do not have this orientation. Additionally, the dark field image reveals areas that would not be obviously identifiable otherwise as crystallites.

Polyhedra and Valence. The characteristic Raman symmetric stretch resonances of $Q^4{}_4$ and $Q^0{}_3$ tellurite polyhedra at 680 and 750 cm^{-1}, respectively, show that as the glass is subjected to heat treatment the tellurite network undergoes relinking (Figure 12).[27] The $Q^0{}_3$ is the isolated $TeO_3{}^{-2}$ unit. This species generally increases as the network is cleaved by the addition of alkali. The $Q^4{}_4$ unit is the TeO_4 unit where all oxygens are connected to the network. The change in relative concentration of these moieties is a typical consequence of annealing of a glass.[28] The symmetric stretch modes of the symmetric and asymmetric niobate polyhedra at 450 and 890 cm^{-1} appear to narrow and attenuate.[29] This result makes conclusions about the changes of the niobate sites difficult without additional information.

^{93}Nb NMR results show the effect of niobate polyhedron geometry and tellurium valence (Figure 11). $KNbTeO_6$ is a pyrochlore with a cubic cell. The NbO_6 octahedron is corner-shared with $Te^{VI}O_6$ octahedra.[30] The higher charge of this neighbor (as compared to Nb^V) has a withdrawing effect on the electrons in the NbO_6 polyhedron and shifts the resonance downfield. Nb_2O_5 is composed of corner-shared layers of edge-shared octahedra.[31] The Nb^V ions are slightly off-center in this material. In $KNbO_3$, the polyhedra are corner-shared, and the Nb^V ions are far from the center of the unit.[32] It is seen that as the glass changes into glass ceramic, the resonance shifts from low field to high field. This effect is due to the change in local symmetry at some atom sites since the energy of the NbO_6 polyhedron is minimized when the cation is off-center. It can also be determined that the predominant Te−O−Nb linkages must be between Te^{IV} and Nb^V in the glass ceramic since the NMR signal behaves oppositely to how it would if oxidation were an important consideration for the structural evolution.

Structure and Theory of Optical Response. The theory of Lines states that asymmetry of the d-metal oxide polyhedra leads to SHG.[10] In a glass that contains d-metal oxides, there are many asymmetric polyhedra, but the isotropic nature of the material effectively cancels out any net frequency doubling. When the polyhedra are ordered, as in the ceramic phase of this material, such distortions will become relevant again, as long as they are not ordered in such a way as to cancel each other out. We see in this material's crystallites two distortions consistent with Lines's theory. The NbO_6 octahedra are asymmetric, and there exists oxide disorder as revealed by scattering analysis. We cannot prove that the space group of this crystal structure is noncentrosymmetric, but the generation of an optical second harmonic has been used for decades in crystallography as evidence for this.[33,34] Indeed, admitting this possibility is reasonable. The arrangement of ions in a glass can be more or less ordered, but a material is only a glass if it lacks long-range order.

(25) Hastings, J. B.; Tomlinson, W.; Cox, D. E. *J. Appl. Crystallogr.* **1983**, *17*, 85.
(26) Vogel, W. *Glass Chemistry*, 2nd ed.; Springer-Verlag: Berlin, 1992.
(27) Heo, J.; Lam, D.; G H Siegel, J.; Mendoza, E. A.; Hensley, D. A. *J. Am. Ceram. Soc.* **1992**, *75*, 1774.
(28) Paul, A. *Chemistry of Glasses*, 2nd ed.; St. Edmundsbury Press: Bury St. Edmonds, 1990.
(29) Jehng, J.-M.; Wachs, I. E. *Chem. Mater.* **1991**, *3*, 100.
(30) Darriet, B. *Mater. Res. Bull.* **1971**, *6*, 1305.
(31) Wells, A. F. *Structural Inorganic Chemistry*, 5th ed.; Oxford Science Publications: London, 1984.
(32) Katz, L.; Megaw, H. D. *Acta Crystallogr.* **1967**, *22*, 639.
(33) Giacovazzo, C.; Monaco, H. L.; Viterbo, D.; Scordari, F.; Gilli, G.; Zanotti, G.; Catti, M. *Fundamentals of Crystallography*, 1st ed.; Oxford University Press: Oxford, 1992; Vol. 2.
(34) Nye, J. F. *Physical properties of crystals, their representation by tensors and matrixes*; Clarendon Press: Oxford, 1969.

The ceramic phase of potassium niobate tellurite glass ceramic arises with little attendant diffusion. It is reasonable to propose that the crystal phase lacks the type of ion ordering necessary for the condition of inversion symmetry. Thus, the response of this d-metal oxide glass ceramic can be understood in terms of this theory.

5. Conclusions

We have shown that neutron scattering reveals additional low-angle peaks in the diffraction pattern of potassium niobate tellurite glass ceramic. Using both these peaks and the peaks from X-ray diffraction, we index the crystalline phase to an orthorhombic cell of $a = 3.39$ Å, $b = 4.78$ Å, and $c = 6.38$ Å; this allows the possibility of a crystalline phase that lacks an inversion center. This unit cell, and real space analysis, permits us to confidently reject the fluorite model previously proposed. Further, we have developed a model of oxide disorder and found asymmetry in the metal oxide polyhedra. These findings together allow the understanding of SHG from this glass ceramic with established theory. We have also shown that oxidation of Te does not play an important role in the development of SHG activity in this material.

Studying the microstructure of the glass and glass ceramic makes it clear why the crystallites do not continue to grow with increased heat treatment time. The glass is phase-separated, and this microstructure determines the ultimate size of the crystallites.

Acknowledgment. This work is supported under NSF Grant DMR-9870246. Major instrumentation has been provided by the NSF-CRIF program (CHE-0077942) and NSF-IMR program (DMR-9802844). Use of the Intense Pulsed Neutron Source and Advanced Photon Source was supported by the U.S. Department of Energy, Basic Energy Sciences, Office of Science, under Contract W-31-109-Eng.-38 with Argonne National Laboratory. The authors wish to thank the staff of the IPNS, especially Mrs. Nicole Murphy and Drs. Chris Benmore and Jim Richardson for helpful discussions and assistance. We acknowledge Dr. John Bollinger from the Indiana University Molecular Structure Center for the X-ray data and useful comments and thank Dr. Peter Lee at APS for his assistance. R.T.H. and B.J.K. are supported by Graduate Assistance in Areas of National Need (GAANN) Fellowships administered by the Department of Education.

CM020615Q